Supporting Information

Rationally Designed Metallic Reentrant Superomniphobic Structures toward Anti-Icing for Low-Surface-Tension Liquids

Daizhou Li[1], Rui Peng[1], Ziyan Song[1], Zhao Liu[1], Zhixuan Chang[1], Hongjun Zhang[1], Peixun Fan[1] and Minlin Zhong[1]**

Laser Materials Processing Research Center
Key Laboratory for Advanced Materials Processing Technology (Ministry of Education)
Joint Research Center for Advanced Materials & Anti-icing of Tsinghua University (SMSE)-AVIC ARI
School of Materials Science and Engineering
Tsinghua University
Beijing 100084, P. R. China
E-mail: fanpeixun@tsinghua.edu.cn, zhml@tsinghua.edu.cn

Contents:

1. Supplementary Discussion

1.1 Thermodynamic analysis of droplet wetting transition on micro-nanostructured surfaces

Maintaining a droplet in the Cassie-Baxter (CB) state is a prerequisite for effective anti-icing on superhydrophobic surfaces. At room temperature, the stability of the CB state can be equivalently described as the energy barrier that must be overcome for the droplet to transition from the CB state to the Wenzel state. To elucidate the influence of droplet surface tension on the stability of the CB state, we analyzed the thermodynamic energy changes during the wetting transition of a droplet on a micro-nanostructured surface. Here, we assume the entire solid-liquid-gas system is isothermal, and the gas within the system satisfies the ideal gas law. Using a classic cylindrical hierarchical micro-nanostructure as the model, the total free energy of the system can be expressed as:[1]

$$G_{\mathrm{T}} = \gamma_{\mathrm{LV}} S_{\mathrm{LV}} + \gamma_{\mathrm{SL}} S_{\mathrm{SL}} + \gamma_{\mathrm{SV}} S_{\mathrm{SV}} + G_{\mathrm{air}} \tag{S1}$$

$$G_{\mathrm{air}} = G_{\mathrm{P_0}} + \int_{\mathrm{P_0}}^{\mathrm{P_1}} V \, dP \tag{S2}$$

where G represents the total free energy of the system; G_{air} denotes the energy of the gas within the air pocket; $G_{\mathrm{P_0}}$ is the free energy of the gas in its initial state within the air pocket; γ_{LV}, γ_{SL}, and γ_{SV} represent the liquid-vapor, solid-liquid, and solid-vapor surface tensions, respectively; S_{LV}, S_{SL}, and S_{SV} are the areas of the liquid-vapor, solid-liquid, and solid-vapor interfaces, respectively; P_0 and P_1 are the initial and final pressures of the gas in the air pocket, respectively; and V is the volume of the air pocket. The initial pressure of the gas in the air pocket equals the ambient pressure. Assuming the free energy of the system in the initial state is G_0, the free energy of the system in its current state after changes is:

$$G_{\mathrm{T}} = G_0 + \gamma_{\mathrm{LV}} \Delta S_{\mathrm{LV}} + \gamma_{\mathrm{SL}} \Delta S_{\mathrm{SL}} + \gamma_{\mathrm{SV}} \Delta S_{\mathrm{SV}} + nRT \cdot \ln \frac{V_0}{V_1} \tag{S3}$$

where ΔS_{LV}, ΔS_{SL}, and ΔS_{SV} represent the changes in the liquid-vapor, solid-liquid, and solid-vapor interfacial areas, respectively; *n* is the amount of substance of the gas; *R* is the ideal gas constant; *T* is the ambient temperature; V_0 and V_1 are the initial and final volumes of the air pocket, respectively. To simplify the subsequent derivation, the analysis is first conducted based on an equivalent closed pore structure. The transition of a droplet from the CB state to the Wenzel state on this structure primarily involves three stages: (1) Pinning of the triple-phase contact line (TPCL) and protruding of the liquid-vapor interface; (2) downward movement of the TPCL until it touches the bottom of the micro-nanostructural gaps; and (3) microstructures are fully wetted, with gas escaping or dissolving into the droplet.[2] In the first stage, the TPCL is pinned at the top edge of the microstructures, and the liquid-vapor interface gradually bulges downward. At this point, the droplet is in the CB state, and the system's free energy can be expressed as:

$$G_1 = G_0 + N\pi r^2 \gamma_{\mathrm{LV}} \cdot \left[\frac{1-\sin\theta}{1+sin\theta} + \frac{P_0 H}{\gamma_{\mathrm{LV}}} \ln\left(\frac{H}{H-H_{\mathrm{a1}}}\right)\right] \tag{S4}$$

$$H_{\mathrm{a1}} = \frac{r(2-3\sin\theta+sin^3\theta)}{-3cos^3\theta} \tag{S5}$$

where *N* is the number of structural units beneath the droplet; *H* is the height of the microstructure; *r* is the radius of the pore structure; H_{a1} is the average protrusion depth of the droplet when pinned at the top; and θ is the sag angle of the liquid-vapor interface. As the liquid-vapor interface continues to sag, θ continuously increases. When the sag angle θ reaches the apparent advancing contact angle θ_{adv} of the microstructure sidewall, the TPCL begins to move downward. At this point, the droplet transitions from the CB state towards the Wenzel state. Due to the small contact angle hysteresis of the nanostructure, its apparent contact angle θ_{ca} can be considered equal to the apparent advancing angle θ_{adv}. $\cos\theta_{\mathrm{adv}} = f_2\,(1+\cos\theta_{\mathrm{Y}}) - 1$; θ_{Y} is the contact angle of the liquid on the smooth sidewall of the

microstructure; f_1 and f_2 are the area fractions of the microstructures and nanostructures, respectively. Consequently, the free energy of the system in the second stage is expressed as:

$$G_2 = G_0 + N\pi r^2\gamma_{\mathrm{LV}} \cdot \left[\frac{1-\sin\theta_{\mathrm{adv}}}{1+\sin\theta_{\mathrm{adv}}} - \left(\frac{2h_1}{r}\right)(f_2 cos\theta_{\mathrm{Y}} + f_2 - 1) + \right.$$

$$\left.\frac{P_0 H}{\gamma_{\mathrm{LV}}} \ln\left(\frac{H}{H-h_1-(H_{\mathrm{a1}})_{\max}}\right)\right] \tag{S6}$$

Here, h_1 denotes the depth of the downward movement of the TPCL; when $\theta = \theta_{\mathrm{adv}}$, H_{a1} reaches its maximum value, $(H_{\mathrm{a1}})_{\max} = \frac{r(2-3\sin\theta_{\mathrm{adv}}+sin^3\theta_{\mathrm{adv}})}{-3cos^3\theta_{\mathrm{adv}}}$. Once the liquid-vapor interface touches the bottom of the microstructure gaps, the gas in the air pocket rapidly escapes or dissolves, ultimately leading to the complete wetting of the microstructures by the droplet. The system is now in the Wenzel state. Correspondingly, its free energy can be expressed as:

$$G_3 = G_0 - N\pi r^2\gamma_{\mathrm{LV}} \cdot \left[1 + \left(1 + \frac{2H}{r}\right) \cdot (f_2 cos\theta_{\mathrm{Y}} + f_2 - 1)\right] - G_{\mathrm{P_0}} \tag{S7}$$

To more intuitively demonstrate the influence of liquid surface tension on the wetting transition barrier, the aforementioned free energy equations were nondimensionalized:

$$G_{\mathrm{T}}^* = \frac{\alpha(G-G_0)(1-f_1)}{N\pi r^2\gamma_{\mathrm{w}}} \tag{S8}$$

Combining Equations S4-S7 with Equation S8, the nondimensionalized total free energy during the droplet transition from the CB state to the Wenzel state can be calculated as follows:

$$G_{\mathrm{T}}^* = \begin{cases} (1-f_1) \cdot \frac{\alpha\gamma_{\mathrm{LV}}}{\gamma_{\mathrm{w}}}\left[\frac{1-sin\theta}{1+sin\theta} + \frac{P_0 H}{\gamma_{\mathrm{LV}}} ln\left(\frac{H}{H-H_{\mathrm{a1}}}\right)\right], & \left(\frac{\pi}{2} \le \theta < \theta_{\mathrm{adv}}\right) \\ (1-f_1) \cdot \frac{\alpha\gamma_{\mathrm{LV}}}{\gamma_{\mathrm{w}}}\left[\frac{1-sin\,\theta_{\mathrm{adv}}}{1+sin\,\theta_{\mathrm{adv}}} - \left(\frac{2h_1}{r}\right)(f_2 cos\theta_{\mathrm{Y}} + f_2 - 1) + \frac{P_0 H}{\gamma_{\mathrm{LV}}} ln\left(\frac{H}{H-h_1-(H_{\mathrm{a1}})_{\max}}\right)\right], \\ \quad (\theta = \theta_{\mathrm{adv}},\ 0 \le h_1 \le H - (H_{\mathrm{m}})_{\max}) \\ -(1-f_1) \cdot \frac{\alpha\gamma_{\mathrm{LV}}}{\gamma_{\mathrm{w}}}\left[1 + \left(\frac{r+2H}{r}\right) \cdot (f_2 cos\theta_{\mathrm{Y}} + f_2 - 1)\right] - \frac{P_0 H(1-f_1)}{\gamma_{\mathrm{w}}}, & (h_1 = H) \end{cases} \tag{S9}$$

where G_{T}^{*} is the nondimensionalized free energy of the system; $(H_{\mathrm{m}})_{\max}$ is the maximum value of meniscus height H_{m}, $(H_{\mathrm{m}})_{\max}=\frac{r(sin\theta_{\mathrm{adv}}-1)}{cos\theta_{\mathrm{adv}}}$; γ_{w} is the surface tension of the deionized (DI) water droplet; and α is a scaling factor. Based on the above analysis, the energy barrier hindering the transition from the CB to the Wenzel state comprises three parts: the pinning energy barrier of the TPCL; the capillary energy barrier for liquid infiltration; and the energy barrier from the compression of the gas in the air pocket. Thus, the nondimensionalized total energy barrier during the wetting process on the hierarchical pore structure surface can be expressed as:

$$\Delta G_{\mathrm{T}}^{*}=(1-f_1)\cdot\frac{\alpha\gamma_{\mathrm{LV}}}{\gamma_{\mathrm{w}}}\left[\frac{1-sin\,\theta_{\mathrm{adv}}}{1+sin\,\theta_{\mathrm{adv}}}-\frac{2(H-(H_{\mathrm{m}})_{\max})}{r}(f_2cos\theta_{\mathrm{Y}}+f_2-1)+\right.$$

$$\left.\frac{P_0H}{\gamma_{\mathrm{LV}}}ln\left(\frac{H}{H_{\mathrm{m}}-(H_{\mathrm{a1}})_{\max}}\right)\right] \tag{S10}$$

Unlike closed pore structures, pillar structures are directly connected to the ambient atmosphere. Previous studies have demonstrated that hierarchical pillar structures can be approximately equivalent to pore structures.[3] The corresponding effective geometric radius and capillary radius are expressed as:

$$\begin{cases} r_{\mathrm{g}}^{\mathrm{eff}}=(\sqrt{\frac{\pi}{2f_{\mathrm{p}}}}-1)r_{\mathrm{p}} \\ \\ r_{\mathrm{c}}^{\mathrm{eff}}=\frac{1-f_{\mathrm{p}}}{f_{\mathrm{p}}}r_{\mathrm{p}} \end{cases} \tag{S11}$$

where r_p is the radius of the pillar structure, and f_p is the area fraction of the pillar structure. For open structures, the gas in the air pockets can freely exchange with the environment. Owing to this characteristic, the contribution of the entrapped gas can be neglected when determining the wetting transition energy barrier for cylindrical hierarchical structures. In this case, the energy barrier of the wetting process consists of two parts: the meniscus energy barrier and the capillary energy barrier. Combining Equations S10 and S11, the nondimensionalized total

energy barrier for the transition from the CB state to the Wenzel state on this structure surface is obtained as:

$$\Delta G_{\mathrm{P}}^{*} = (1 - f_1) \cdot \frac{\alpha \gamma_{\mathrm{LV}}}{\gamma_{\mathrm{w}}} \left[\frac{1 - \sin\theta_{\mathrm{adv}}}{1 + \sin\theta_{\mathrm{adv}}} - \frac{2\left(H - (H_{\mathrm{m}}^{\mathrm{eff}})_{\max}\right)}{r^{\mathrm{eff}}} (f_2 cos\theta_{\mathrm{Y}} + f_2 - 1) \right] \quad \left(\theta_{\mathrm{adv}} \geq \frac{\pi}{2}\right) \tag{S12}$$

Here, $(H_{\mathrm{m}}^{\mathrm{eff}})_{\max}$ is the maximum effective meniscus height, $(H_{\mathrm{m}}^{\mathrm{eff}})_{\max} = r^{\mathrm{eff}} \cdot \frac{sin\,\theta_{\mathrm{adv}} - 1}{cos\theta_{\mathrm{adv}}}$; r^{eff} is the effective geometric radius corresponding to pillars with diameter r_{p}, $r^{\mathrm{eff}} = (\sqrt{\frac{\pi}{2f_1}} - 1)r_{\mathrm{p}}$. Furthermore, when the liquid surface tension is so low that the apparent advancing angle θ_{adv} is less than $\frac{\pi}{2}$, the above energy barrier calculation formula is no longer applicable. In this case, it is necessary to account for the sign change of the trigonometric functions associated with θ_{adv} and modify the formula based on the upward-concave characteristic of the meniscus. The nondimensionalized total energy barrier for the wetting transition under this condition can be expressed as:

$$\Delta G_{\mathrm{P}}^{*} = (1 - f_1) \cdot \frac{\alpha \gamma_{\mathrm{LV}}}{\gamma_{\mathrm{w}}} \left[\frac{1 - \sin\theta_{\mathrm{adv}}}{1 + \sin\theta_{\mathrm{adv}}} - \frac{2H}{r^{\mathrm{eff}}} (f_2 cos\theta_{\mathrm{Y}} + f_2 - 1) \right] \quad (\theta_{\mathrm{adv}} < \frac{\pi}{2}) \tag{S13}$$

In this study, $f_1 = 0.175$, $f_2 = 0.3$, $\gamma_{\mathrm{w}} = 72.8$ mN·m^{-1}, $\alpha = 10$, $H = 200$ μm, and $r_{\mathrm{p}} = 42.5$ μm. θ_{Y} is the intrinsic contact angle of the liquid on a smooth surface. Given a specific surface material, θ_{Y} is solely determined by the liquid's surface tension γ_{LV}. Therefore, the independent variables in Equations S12 and S13 can be simplified to γ_{LV} and the energy barrier $\Delta G_{\mathrm{P}}^{*}$. This indicates that the liquid surface tension determines the stability of the droplet CB state on the micro-nanostructured surface by influencing the wetting transition energy barrier.

1.2 Energetic analysis of droplet Cassie-Baxter state retention on superhydrophobic surfaces

The stability of the CB state on superhydrophobic surfaces varies for liquids with different surface tensions. The underlying thermodynamic mechanism lies in the principle that system evolution always proceeds from higher-energy states to lower-energy states. The higher the total free energy of the system, the poorer its thermodynamic stability. To clarify the role of surface tension in regulating droplet steady state from a quantitative perspective, we calculated the total free energy of the system when the droplet is in the CB state. Considering the entire interfacial system as an open, isothermal system and neglecting the effects of droplet volume and the gas within the air pocket, the free energy of the system can be expressed as:

$$E_{\mathrm{T}} = \gamma_{\mathrm{LV}} A_{\mathrm{LV}} + \gamma_{\mathrm{SV}} A_{\mathrm{SV}} + \gamma_{\mathrm{SL}} A_{\mathrm{SL}} \tag{S14}$$

$$A_{\mathrm{LV}} = A_{\mathrm{cap}} + \frac{A_0(1-f_{\mathrm{s}})}{cos\phi} \tag{S15}$$

$$A_{\mathrm{SV}} = A_0(1 - f_{\mathrm{s}}) + NHp \tag{S16}$$

$$A_{\mathrm{SL}} = f_{\mathrm{s}} A_0 \tag{S17}$$

where E_{T} is the total free energy of the system; γ_{LV}, γ_{SV}, and γ_{SL} represent the liquid-vapor, solid-vapor, and solid-liquid surface tensions, respectively; A_{LV}, A_{SV}, and A_{SL} denote the areas of the liquid-vapor, solid-vapor, and solid-liquid interfaces, respectively; A_{cap} is the area of the spherical cap formed by the droplet contacting the surface; A_0 is the projected area of the droplet on the surface; f_{s} is the solid-liquid contact area fraction; ϕ is the angle between the meniscus and the horizontal direction; N is the number of structural units beneath the droplet; H is the height of the microstructure; and p is the perimeter of the microstructure cross-section. When a droplet maintains the CB state on a superhydrophobic surface, it simultaneously satisfies Young's equation and capillary force equilibrium, expressed as:

$$\cos\theta_{\mathrm{Y}} = \frac{\gamma_{\mathrm{SV}} - \gamma_{\mathrm{SL}}}{\gamma_{\mathrm{LV}}} \tag{S18}$$

$$\gamma_{\mathrm{LV}} \cdot sin\phi = C_1 \tag{S19}$$

where θ_{Y} is the intrinsic contact angle of the liquid on a smooth surface, and C_1 is a constant. Substituting Equations S15-S19 into Equation S14 and simplifying yields the calculation formula:

$$E_{\mathrm{T}} = \gamma_{\mathrm{LV}}(A_{\mathrm{cap}} + \frac{A_0(1-f_{\mathrm{s}})}{cos\phi} - f_{\mathrm{s}}A_0 cos\theta_{\mathrm{Y}}) + \gamma_{\mathrm{SV}}(A_0 + NHp) \tag{S20}$$

$$K(\gamma_{\mathrm{LV}}) = A_{\mathrm{cap}} + \frac{A_0(1-f_{\mathrm{s}})}{cos\phi} - f_{\mathrm{s}}A_0 cos\theta_{\mathrm{Y}} \tag{S21}$$

$$C_2 = \gamma_{\mathrm{SV}}(A_0 + NHp) \tag{S22}$$

$$E_{\mathrm{T}} = \gamma_{\mathrm{LV}}K(\gamma_{\mathrm{LV}}) + C_2 \tag{S23}$$

Since all parameters in Equation S22 are constants, C_2 is a constant. To elucidate the quantitative relationship between liquid surface tension and system free energy more clearly, we computed the derivative of E_{T} with respect to γ_{LV}, resulting in:

$$\frac{dE_{\mathrm{T}}}{d\gamma_{\mathrm{LV}}} = K(\gamma_{\mathrm{LV}}) + \gamma_{\mathrm{LV}}\frac{dK}{d\gamma_{\mathrm{LV}}} \tag{S24}$$

Combining Equations S18, S19, and S21, substituting into Equation S23, expanding, and simplifying, yields the final expression for the derivative. The derivation process is as follows:

$$\frac{dK}{d\gamma_{\mathrm{LV}}} = \frac{\partial K}{\partial \phi}\frac{d\phi}{d\gamma_{\mathrm{LV}}} + \frac{\partial K}{\partial \theta_{\mathrm{Y}}}\frac{d\theta_{\mathrm{Y}}}{d\gamma_{\mathrm{LV}}} \tag{S25}$$

$$\frac{\partial K}{\partial \phi} = A_0(1-f_{\mathrm{s}})\frac{sin\phi}{cos^2\phi} \tag{S26}$$

$$\frac{d\phi}{d\gamma_{\mathrm{LV}}} = -\frac{sin\phi}{\gamma_{\mathrm{LV}}cos\phi} \tag{S27}$$

$$\frac{\partial K}{\partial \phi}\frac{d\phi}{d\gamma_{\mathrm{LV}}} = -A_0(1-f_{\mathrm{s}})\frac{sin^2\phi}{\gamma_{\mathrm{LV}}cos^3\phi} \tag{S28}$$

$$\frac{\partial K}{\partial \theta_{\mathrm{Y}}} = f_{\mathrm{s}}A_0 sin\theta_{\mathrm{Y}} \tag{S29}$$

$$\frac{d\theta_{\mathrm{Y}}}{d\gamma_{\mathrm{LV}}} = \frac{cos\theta_{\mathrm{Y}}}{\gamma_{\mathrm{LV}}sin\theta_{\mathrm{Y}}} \tag{S30}$$

$$\frac{\partial K}{\partial \theta_{\mathrm{Y}}}\frac{d\theta_{\mathrm{Y}}}{d\gamma_{\mathrm{LV}}} = f_{\mathrm{s}}A_0\frac{cos\theta_{\mathrm{Y}}}{\gamma_{\mathrm{LV}}} \tag{S31}$$

$$\frac{dE_{\mathrm{T}}}{d\gamma_{\mathrm{LV}}} = A_{\mathrm{cap}} + A_0(1 - f_{\mathrm{s}})\frac{cos2\phi}{cos^3\phi} \tag{S32}$$

When the surface tension of the liquid is in a relatively low range, the horizontal inclination angle ϕ of the meniscus approaches $\frac{\pi}{2}$. At this point, $\cos\phi$ approaches 0 and $cos2\phi$ approaches -1. Under this condition, the derivative $\frac{dE_{\mathrm{T}}}{d\gamma_{\mathrm{LV}}} \ll 0$, indicating that the system free energy E_{T} decreases monotonically as the droplet surface tension γ_{LV} increases. Therefore, a droplet with lower surface tension corresponds to a higher energy when maintaining the CB state on the superhydrophobic surface, resulting in correspondingly lower thermodynamic stability for that state.

2. Supplementary Table

Table S1. Detailed process parameters for fabricating different structured surfaces

Types	Processing	Laser Fluence (J cm^{-2})	Scanning Speed (mm s^{-1})	Repetition Frequency	Pulse Duration	Scanning Route	Scanning Pitch (μm)
MA	Laser ablation	15-25	2000-3000	300 kHz	150 ns	Crossed lines	10
MANW	Laser ablation	15-25	2000-3000	300 kHz	150 ns	Crossed lines	10
	Wet chemical reaction	Solution: 2.5 mol L^{-1} NaOH + 0.1 mol L^{-1} $(NH_4)_2S_2O_8$ Temperature: 10-30 ℃ Time: 20-50 min					
MARW	Laser ablation	15-25	2000-3000	300 kHz	150 ns	Crossed lines	10
	Hot pressing	Force: 60-120 N Temperature: 500-800 ℃					
	Wet chemical reaction	Solution: 2.5 mol L^{-1} NaOH + 0.1 mol L^{-1} $(NH_4)_2S_2O_8$ Temperature: 10-30 ℃ Time: 20-50 min					

3. Supplementary Figures

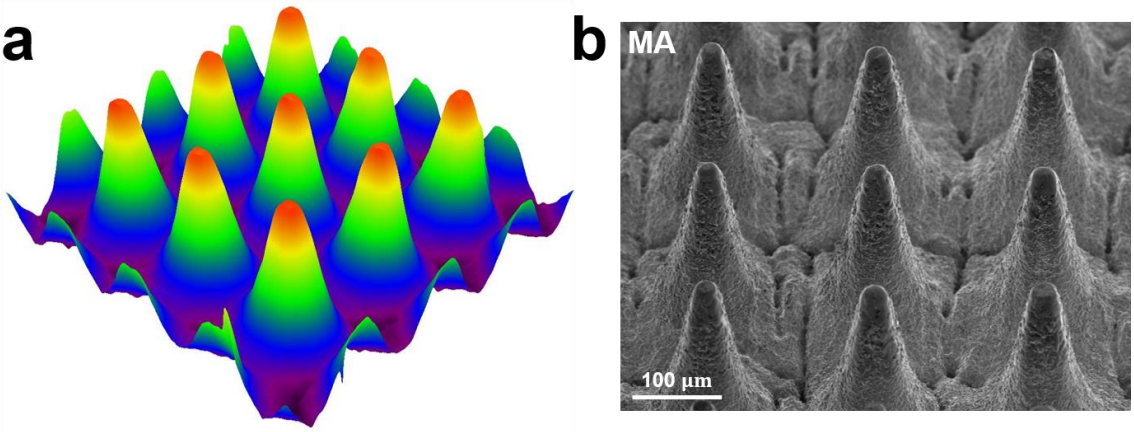

Figure S1. Micromorphology of the laser-fabricated MA. (a) Three-dimensional topography. **(b)** SEM image.

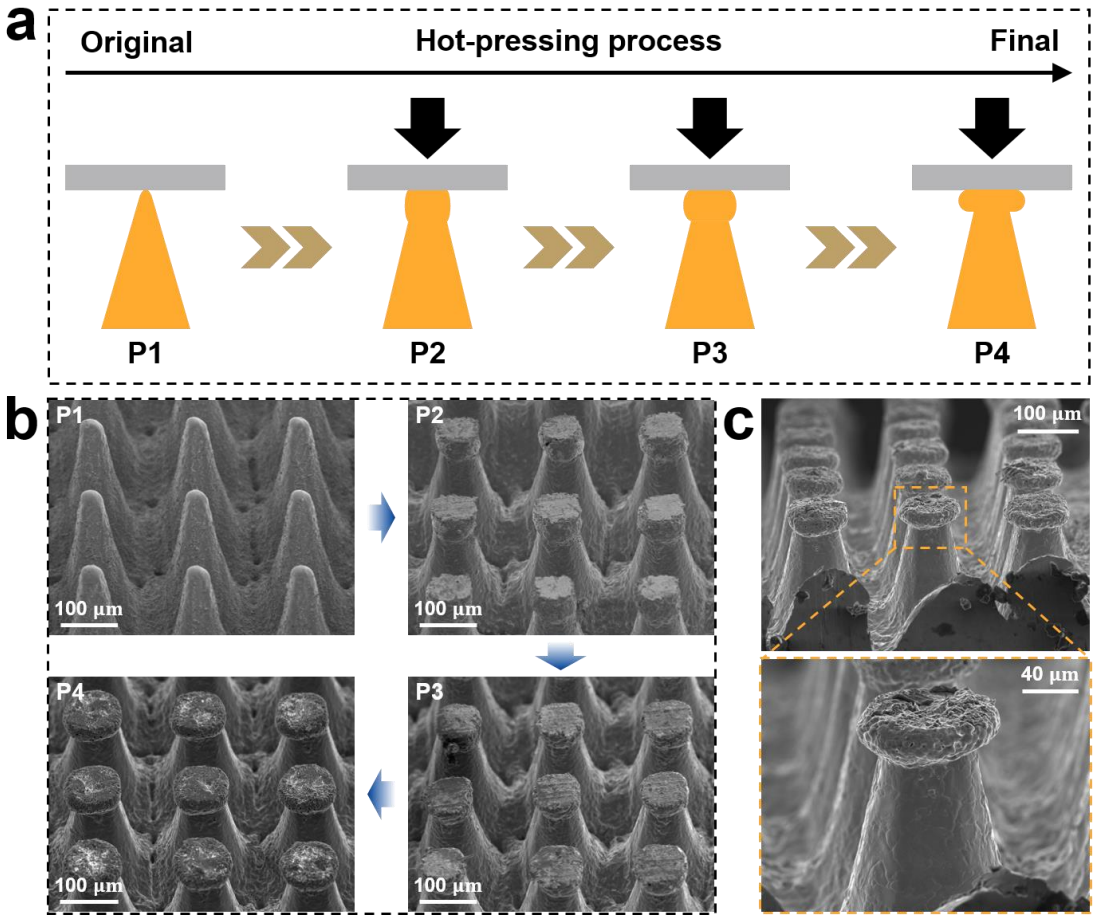

Figure S2. Formation process of the micro reentrant array structure. (a) Schematic of the formation process. **(b)** SEM images captured during formation. **(c)** Magnified side-view image of an individual reentrant structure.

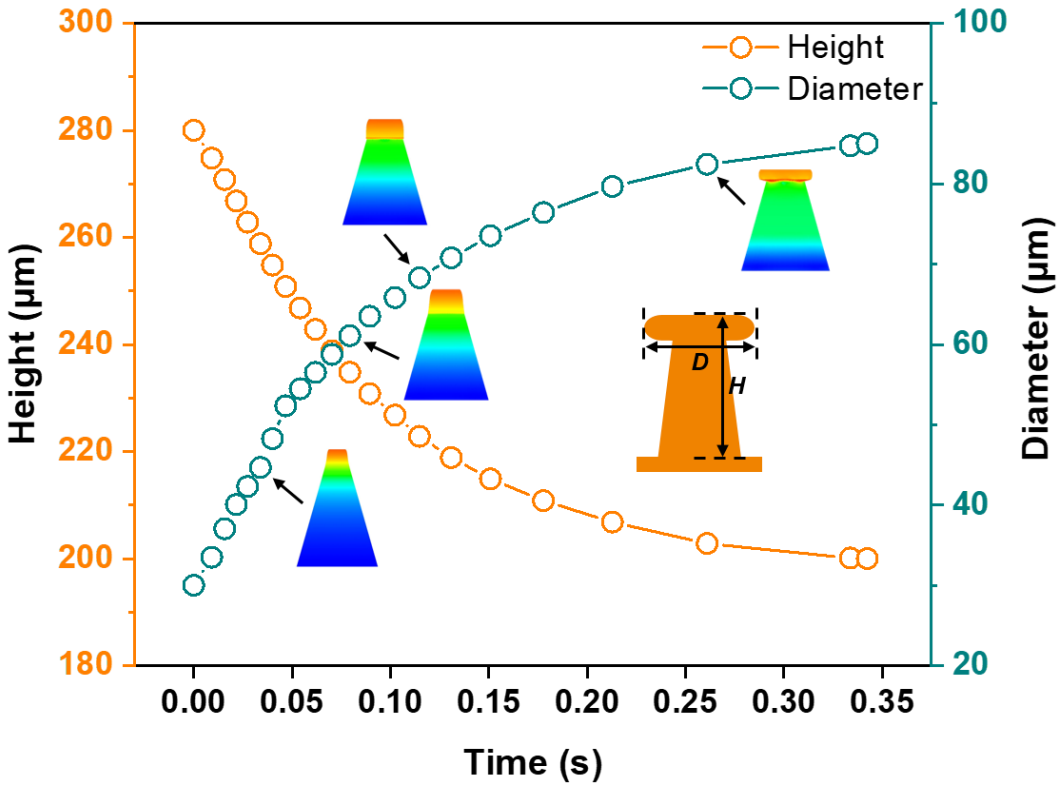

Figure S3. Finite element simulation of the reentrant structure formation process with the temporal evolution of size parameters. The insets show the morphological evolution at different stages (Software: Abaqus).

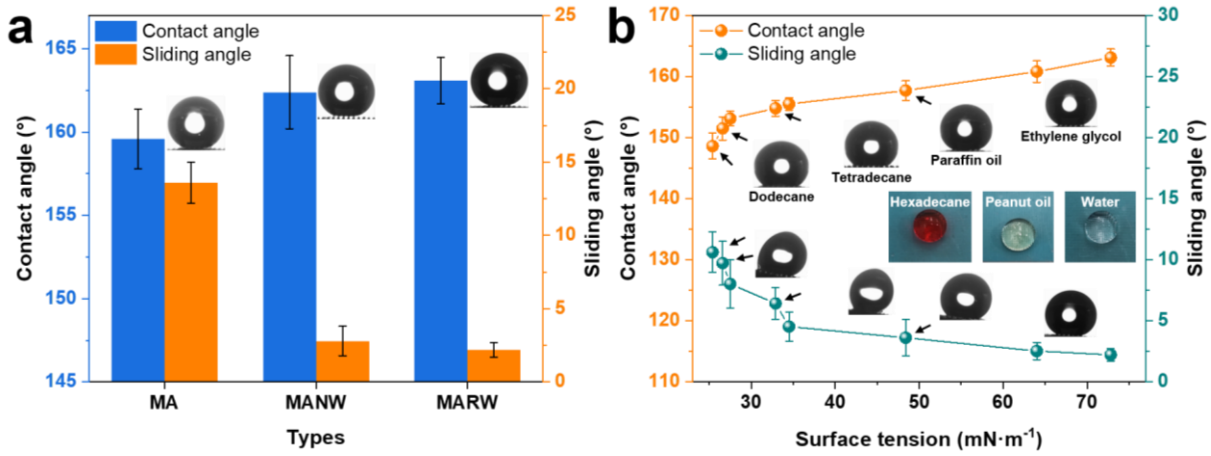

Figure S4. Liquid repellency of the three surfaces at room temperature. (a) Superhydrophobicity of the three surfaces. **(b)** Contact angles and sliding angles of liquids with different surface tensions on the MARW surface. The insets show optical images of hexadecane (red), peanut oil (light yellow), and DI water (transparent) droplets on the MARW surface.

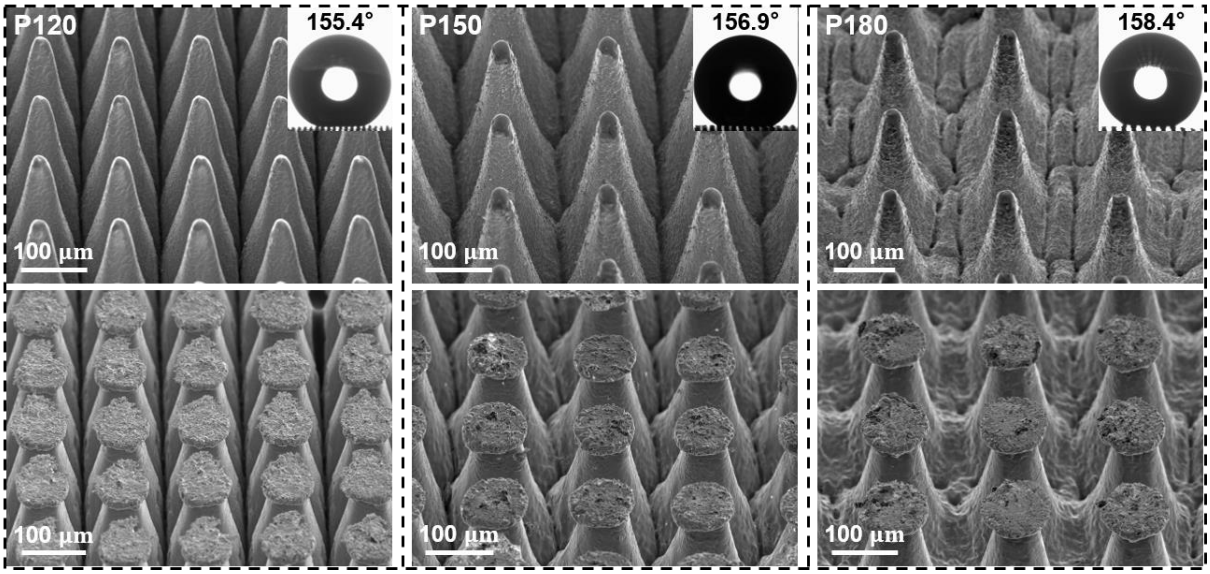

Figure S5. SEM images of MAs with different pitchs before and after hot pressing.

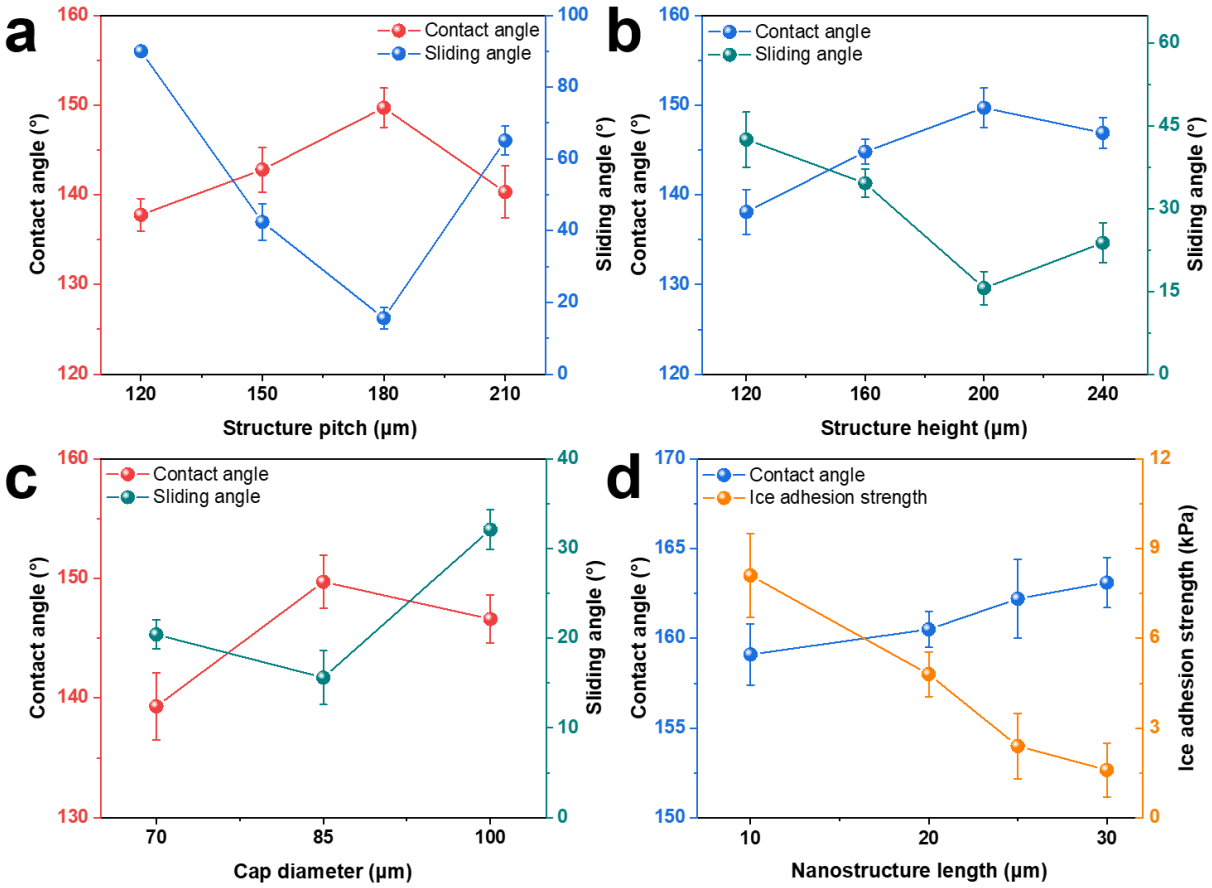

Figure S6. Optimization of structural parameters for the MARW surface. (a-c) Effect of structural parameters on oleophobicity. **(d)** Effect of nanostructure length on superhydrophobicity and ice adhesion strength.

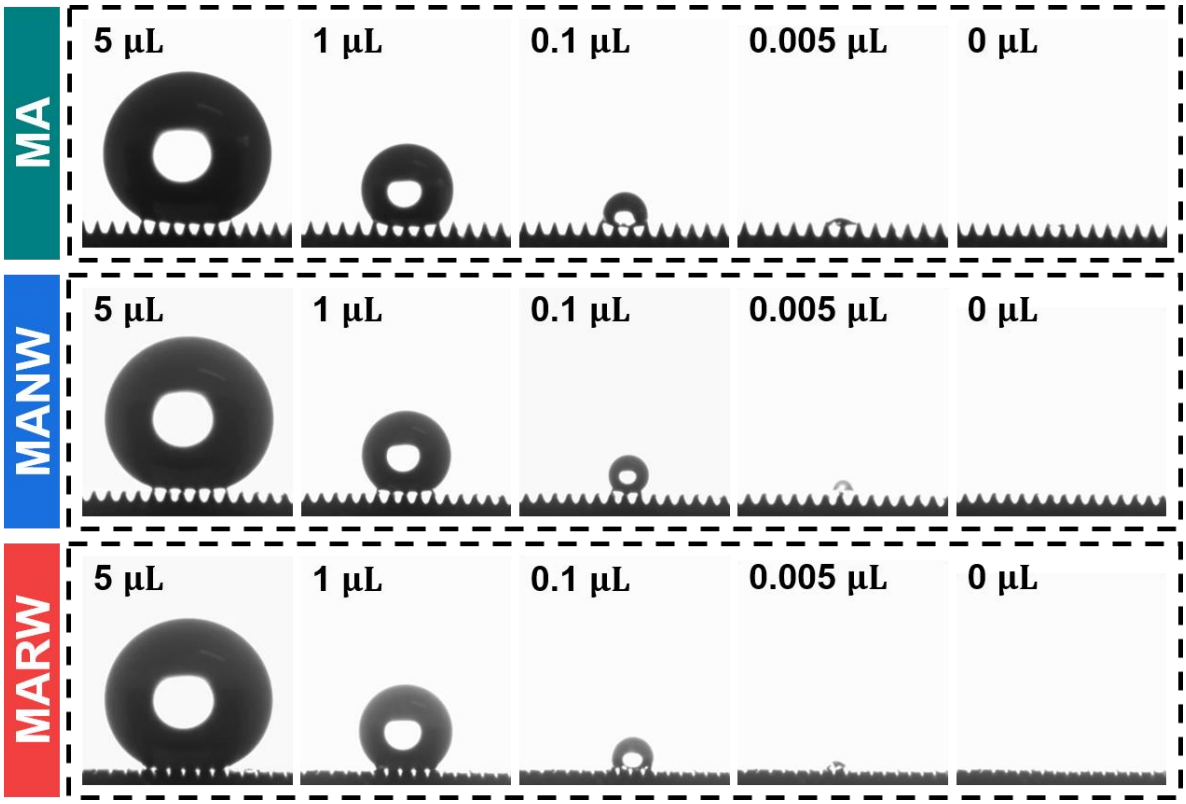

Figure S7. Side-view optical images of the droplet evaporation process on the three surfaces.

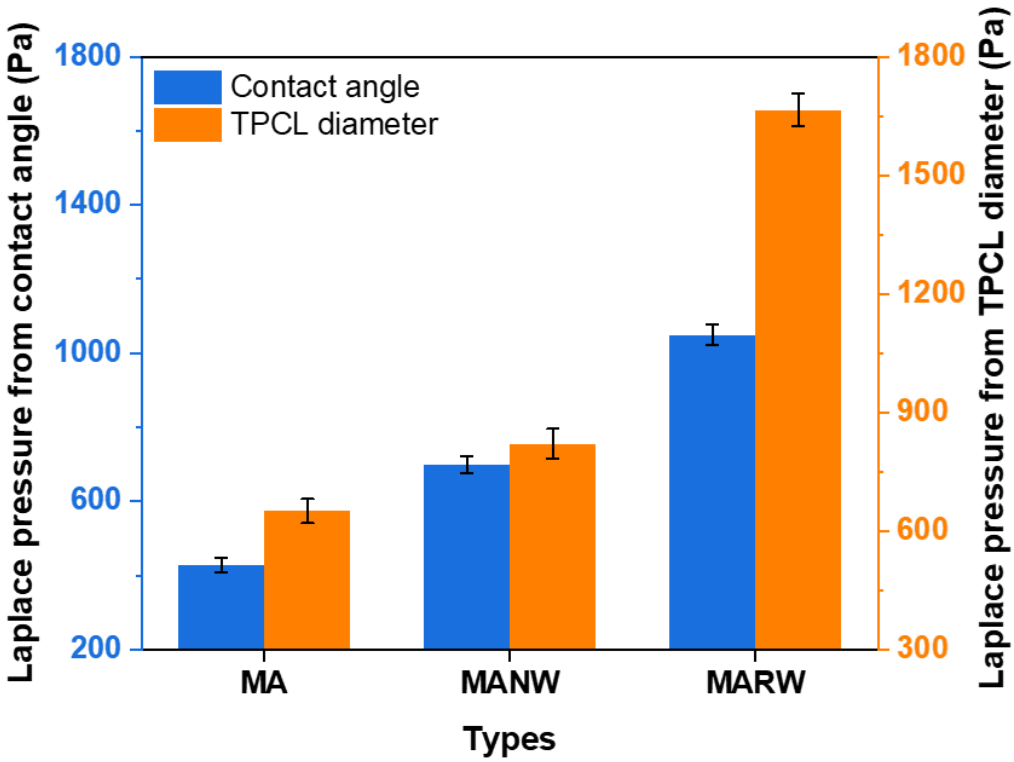

Figure S8. Laplace pressure derived from the contact angle and TPCL diameter on the three surfaces.

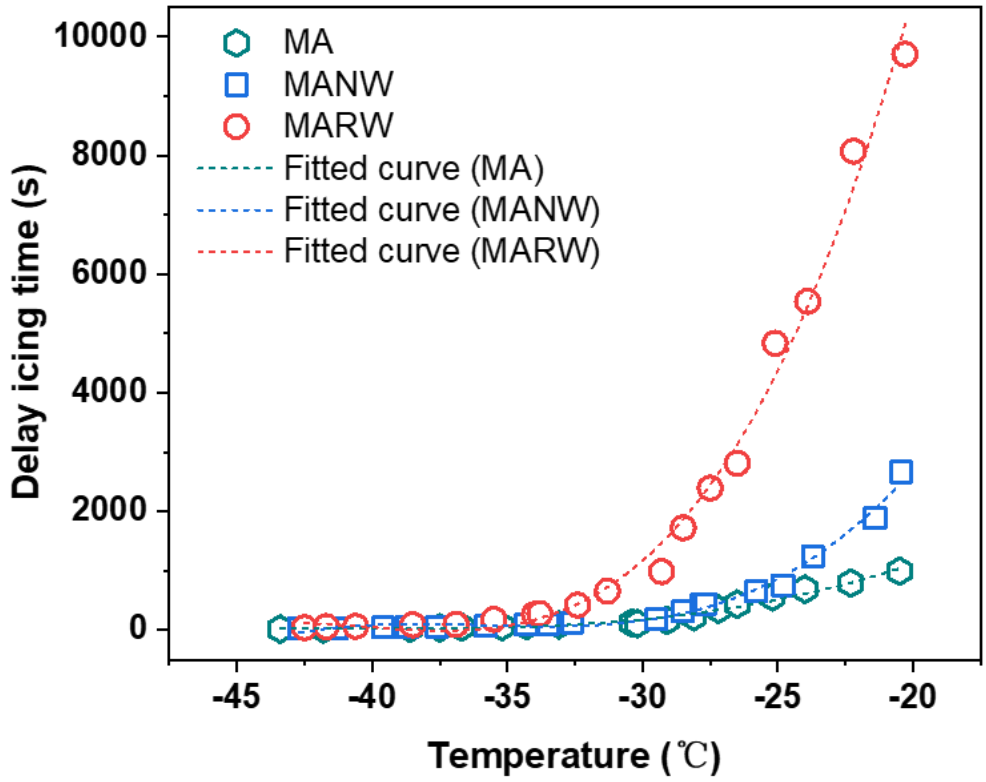

Figure S9. Icing delay time of the three surfaces at different temperatures. The relative humidity was maintained at 70 ±5% RH.

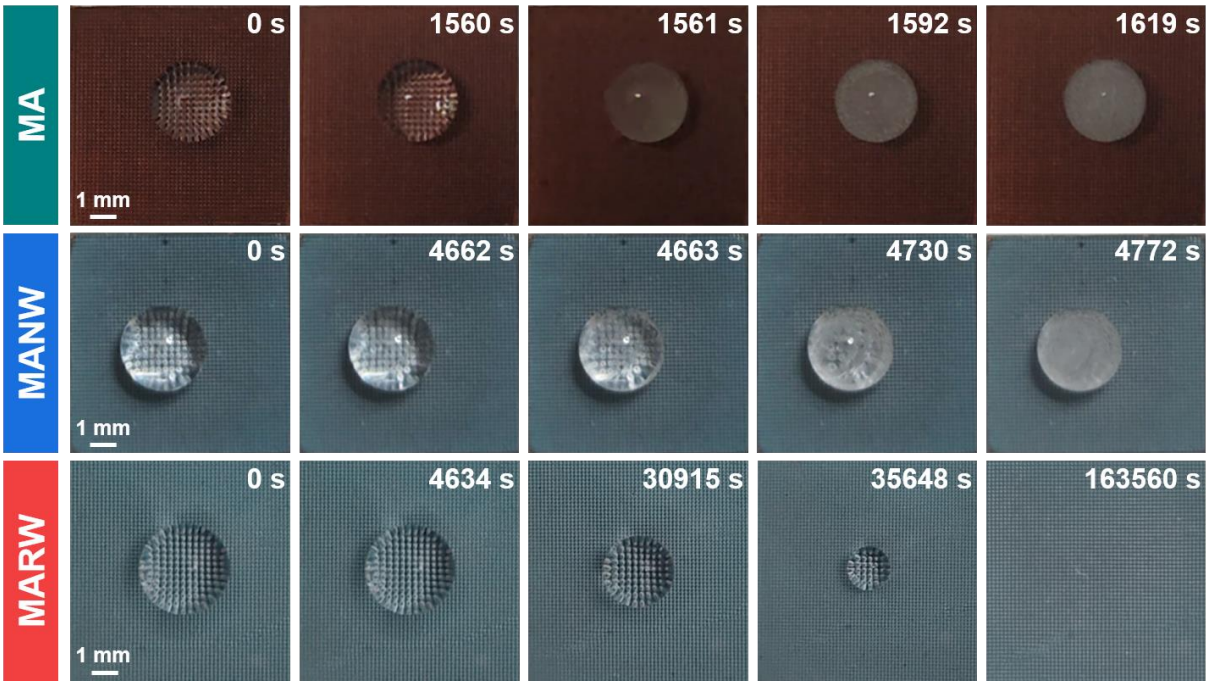

Figure S10. Optical images of droplets at different icing stages on the three surfaces. The ambient temperature and relative humidity were maintained at -17 ±2 ℃ and 70 ±5% RH, respectively.

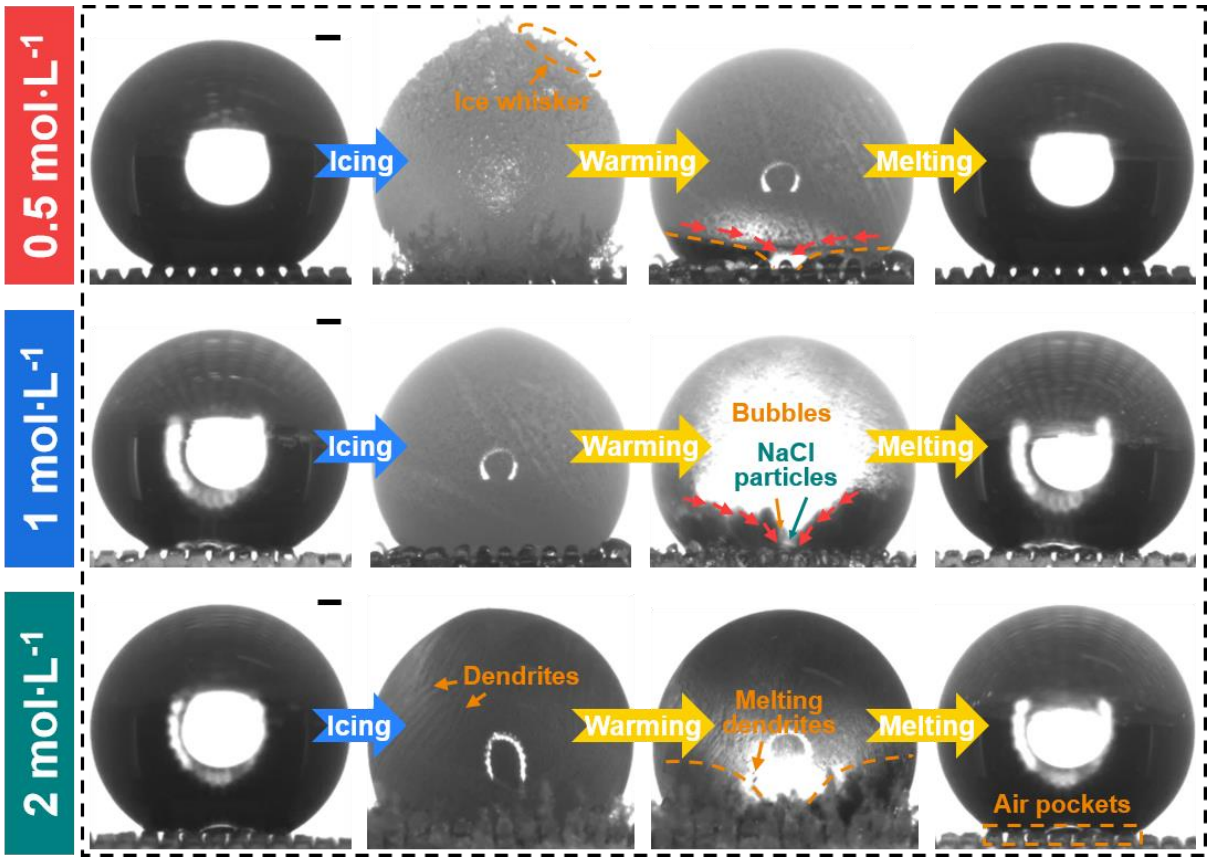

Figure S11. State changes of NaCl droplets at different concentrations on the MARW surface during icing and melting. The scale bar is 200 μm.

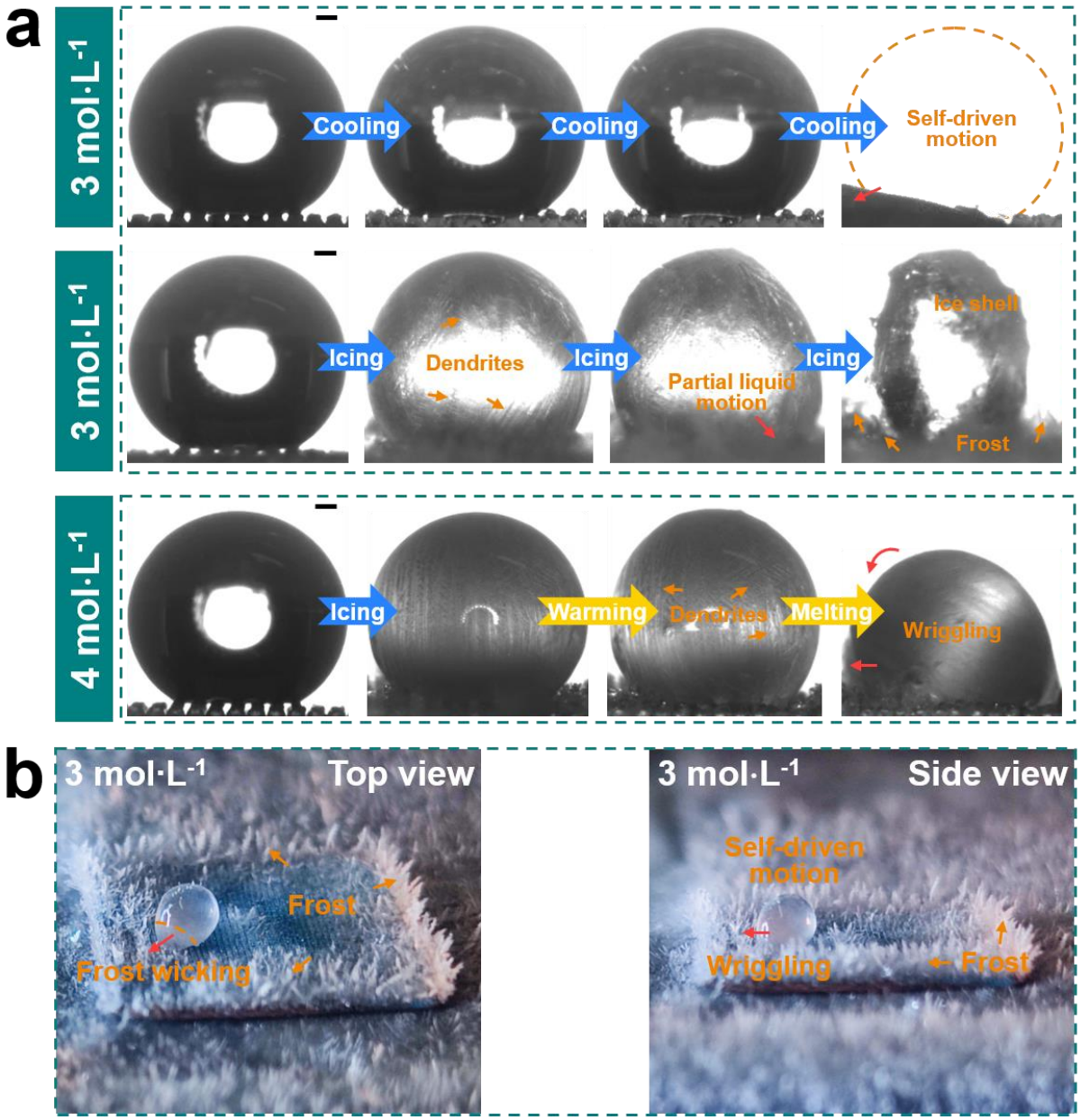

Figure S12. Icing and melting behavior of high-concentration NaCl droplets on the MARW surface. **(a)** Optical images showing state changes of the droplet during icing and melting. The scale bar is 200 μm. **(b)** Top-view and side-view optical photographs of the self-driven motion of the droplet induced by the wicking effect of frost crystals.

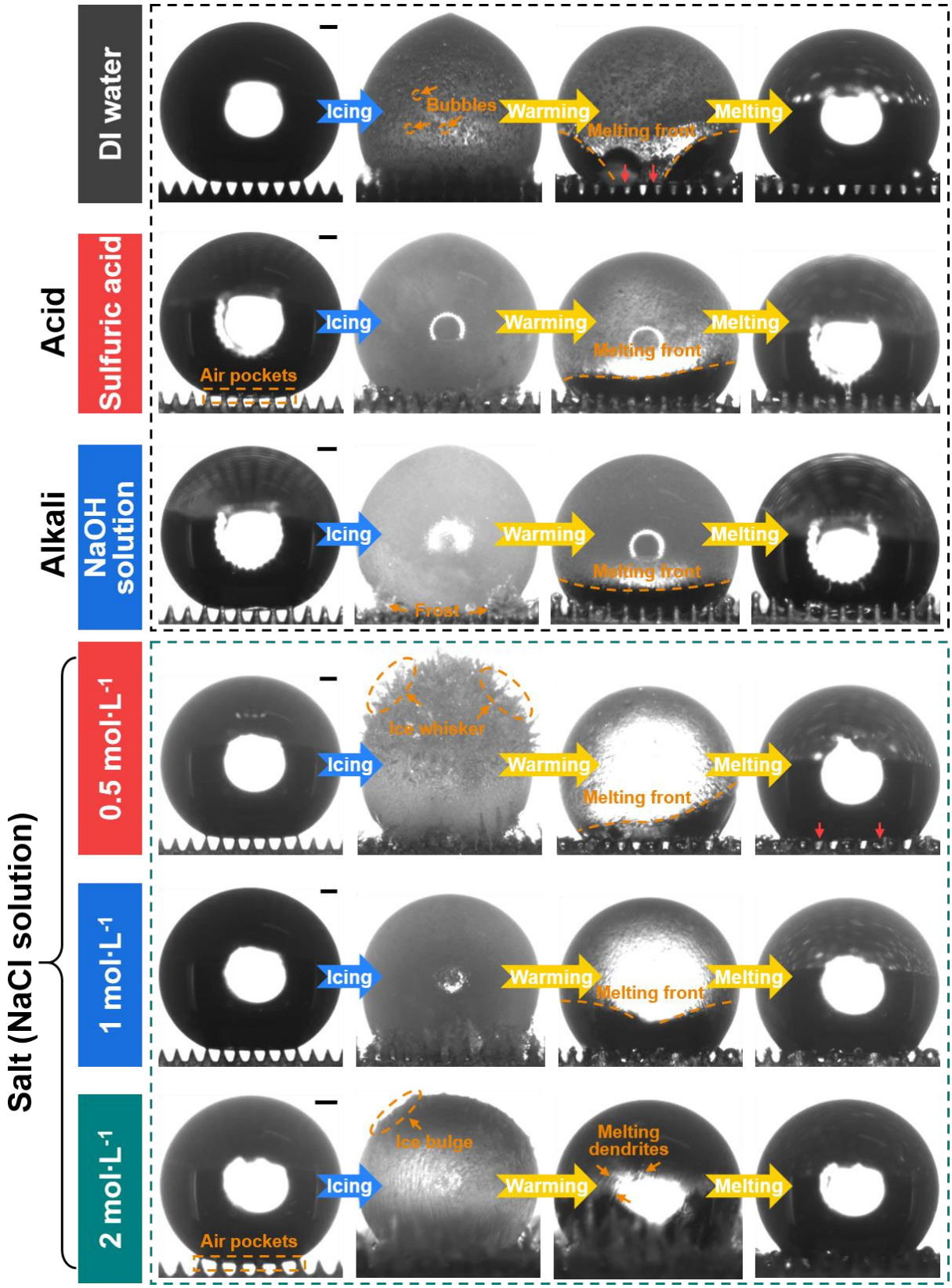

Figure S13. State changes of water, acid, alkali, and salt droplets on the MANW surface during icing and melting. The scale bar is 200 μm.

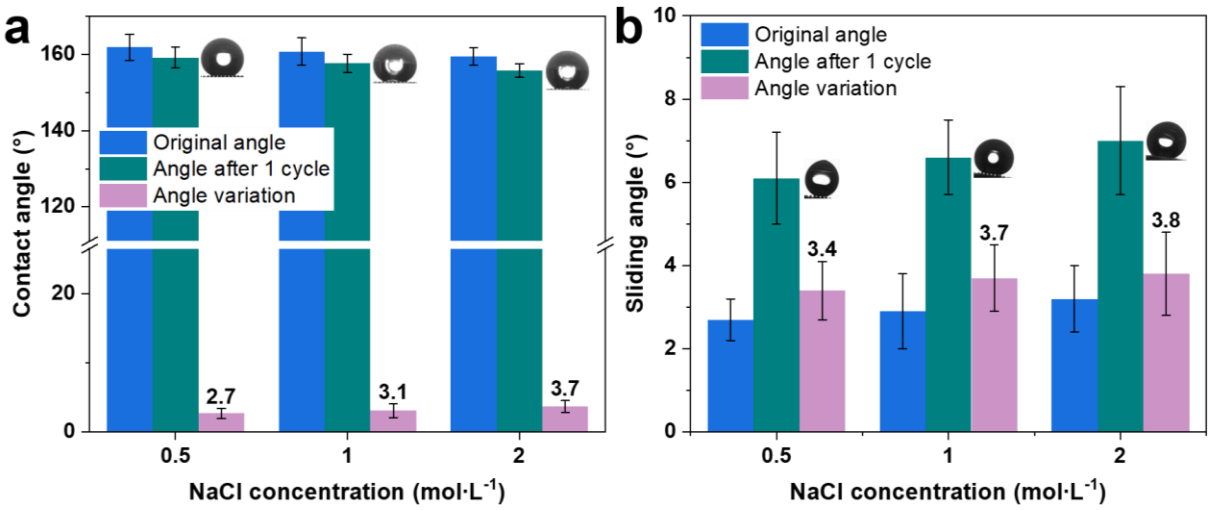

Figure S14. Variations in contact angle and sliding angle of NaCl droplets at different concentrations on the MARW surface after icing-melting cycles. (a) Contact angle. **(b)** Sliding angle.

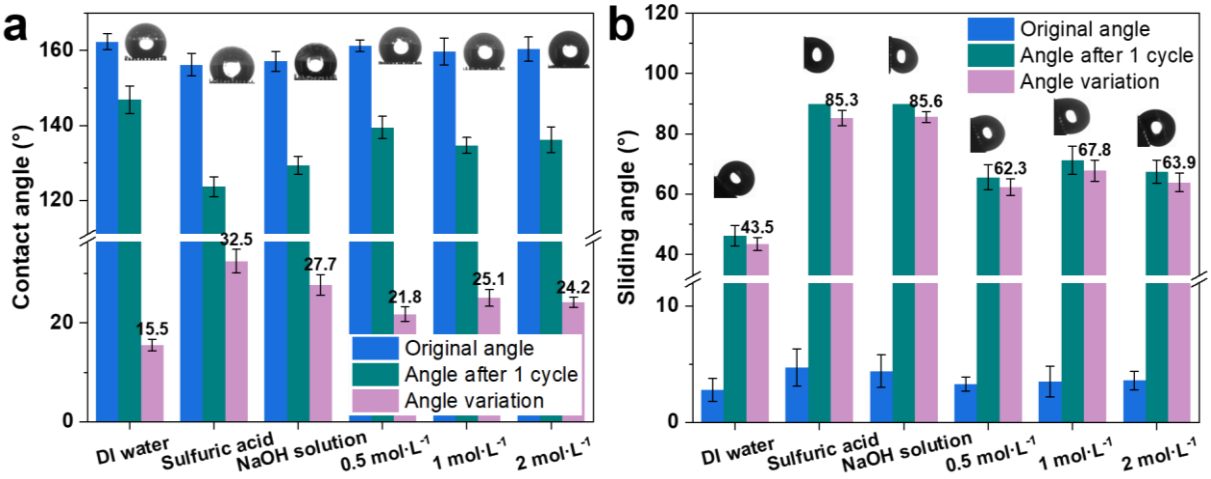

Figure S15. Variations in contact angle and sliding angle of various droplets on the MANW surface after icing-melting cycles. (a) Contact angle. **(b)** Sliding angle.

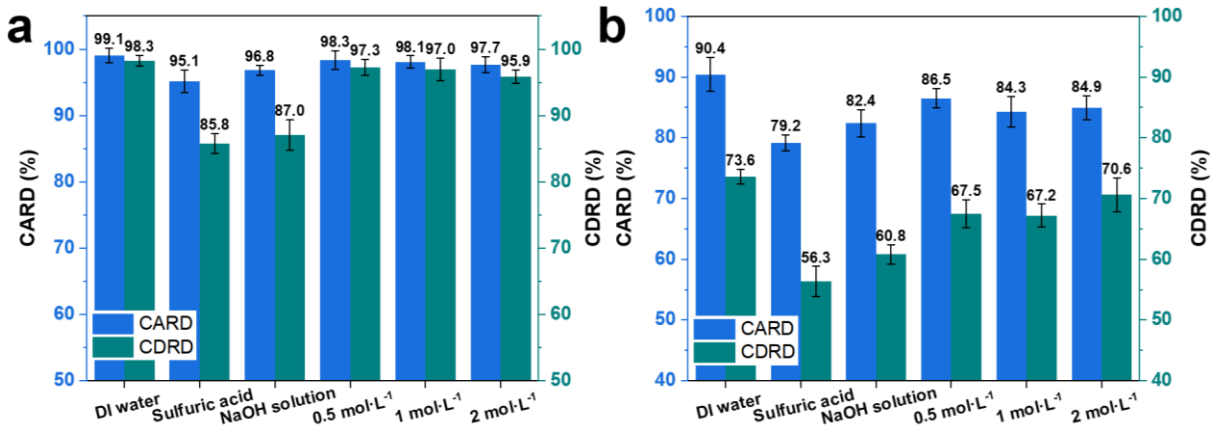

Figure S16. Contact angle retention degree (CARD) and contact diameter retention degree (CDRD) of various droplets on the two surfaces after icing-melting cycles. (a) MARW surface. **(b)** MANW surface. CARD is defined as the percentage of the droplet's contact angle θ_a after icing-melting cycles relative to its initial contact angle θ_b, calculated as $\delta_{CA} = \frac{\theta_a}{\theta_b} \times 100\%$. CDRD is defined as the percentage of the droplet's initial contact diameter D_b relative to its contact diameter D_a after icing-melting cycles, calculated as $\delta_{CD} = \frac{D_b}{D_a} \times 100\%$.

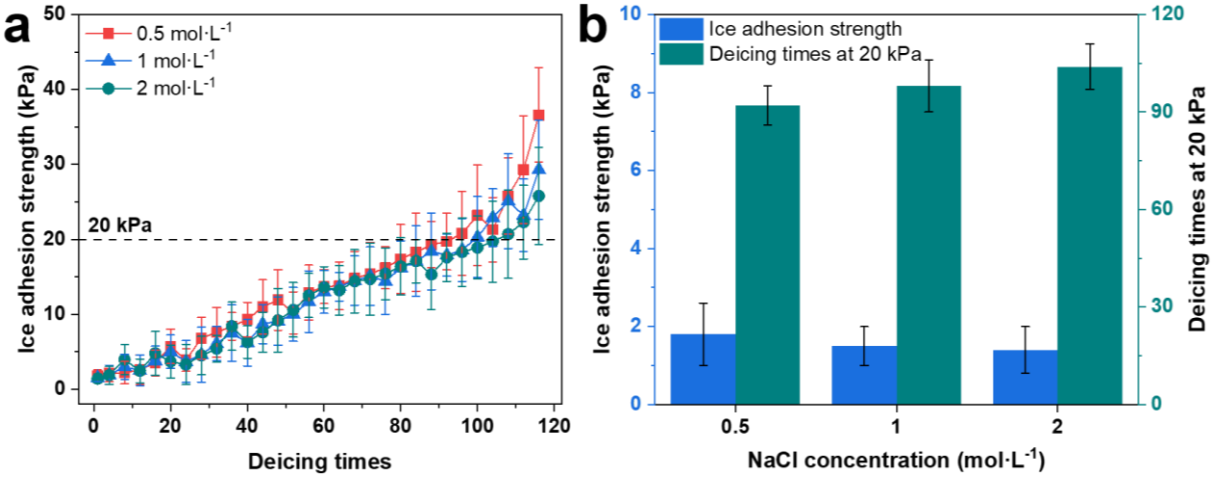

Figure S17. Icephobic performance of the MARW surface against NaCl solutions at different concentrations. (a) Effect of deicing cycles on the ice adhesion strength of NaCl solutions at various concentrations. **(b)** Initial ice adhesion strength of three liquids and the maximum number of deicing cycles achieved while maintaining ice adhesion strength below 20 kPa.

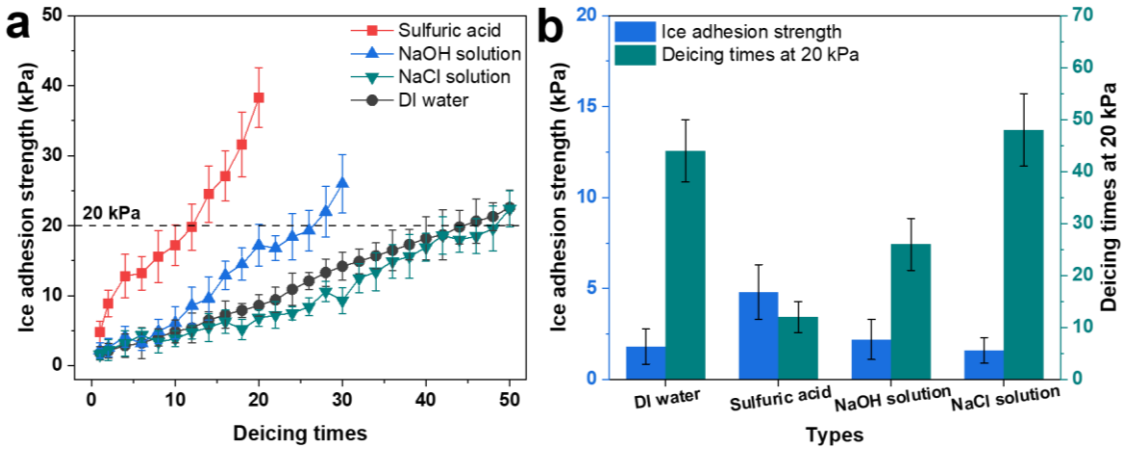

Figure S18. Icephobic performance of the MANW surface against aqueous solutions. (a) Effect of deicing cycles on the ice adhesion strength of four liquids. **(b)** Initial ice adhesion strength of the four liquids and the maximum number of deicing cycles achieved while maintaining ice adhesion strength below 20 kPa. The concentration of the NaCl solution is 1 mol·L^{-1}.

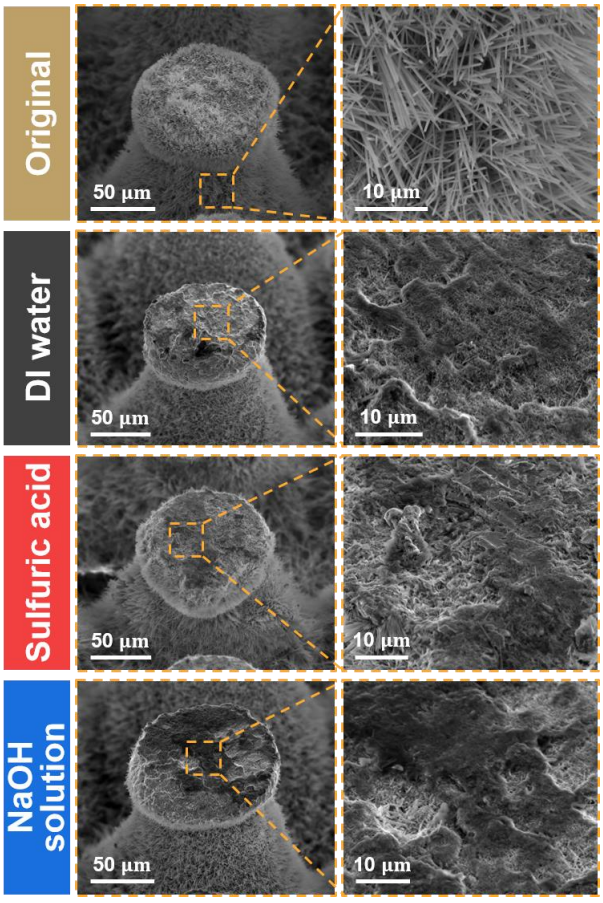

Figure S19. SEM images of the MARW surface in its pristine state and after multiple deicing cycles with three different liquids. The numbers of deicing cycles for water, acid, and alkali solutions were 90, 28, and 52, respectively.

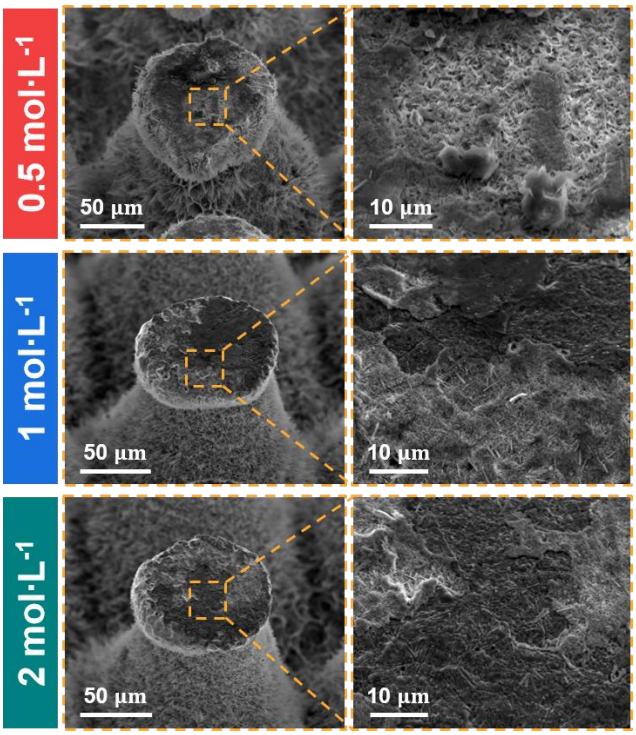

Figure S20. SEM images of the MARW surface after multiple deicing cycles with NaCl solutions at different concentrations. The numbers of deicing cycles for 0.5, 1, and 2 mol·L^{-1} NaCl solutions were 92, 98, and 104, respectively.

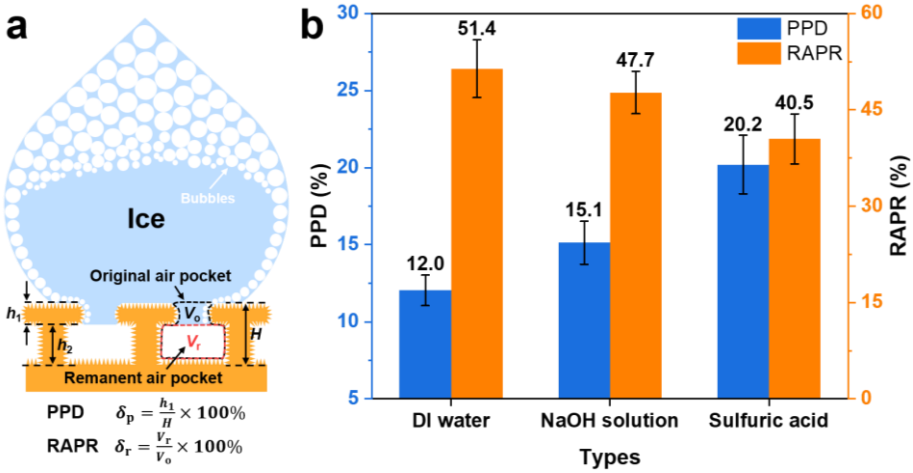

Figure S21. Percentage of pinning depth (PPD) and remaining air pocket volume ratio (RAPR) after freezing for DI water, NaOH solution, and sulfuric acid solution. (a) Schematic diagram of the geometric parameters used for calculating PPD and RAPR. **(b)** PPD and RAPR for three droplets on the MARW surface. PPD represents the pinned depth h_1 of the droplet after freezing as a percentage of the original air pocket height H, calculated as $\delta_p = \frac{h_1}{H} \times 100\%$. RAPR represents the ratio of the remaining air pocket volume V_r after freezing to the original air pocket volume V_o, calculated as $\delta_r = \frac{V_r}{V_o} \times 100\%$.

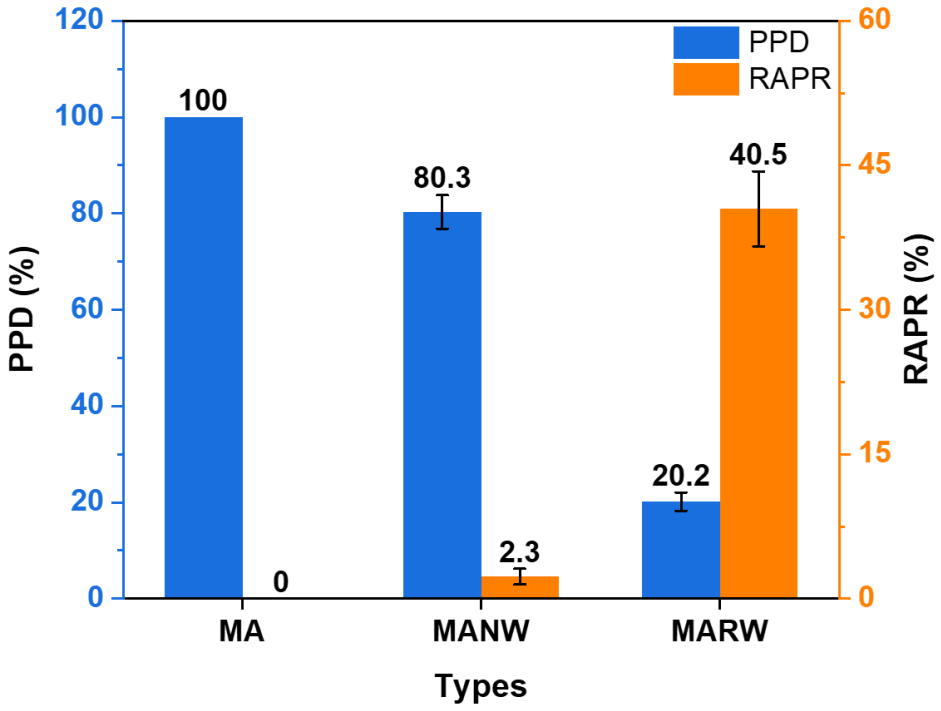

Figure S22. PPD and RAPR of sulfuric acid droplets after freezing on the three surfaces.

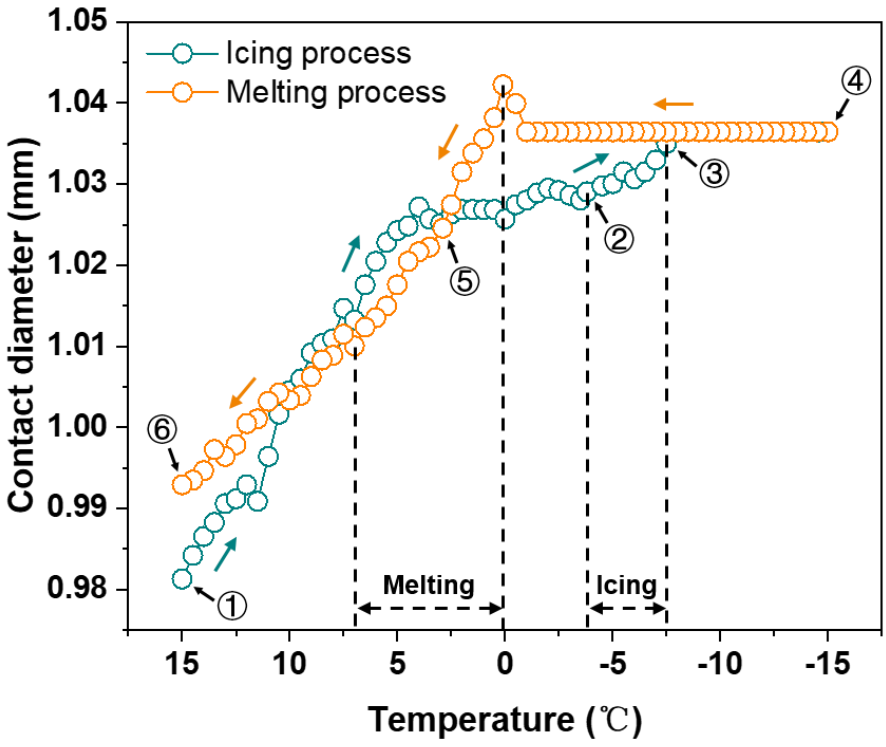

Figure S23. Variation in the contact diameter of a peanut oil droplet on the MARW surface during icing and melting processes.

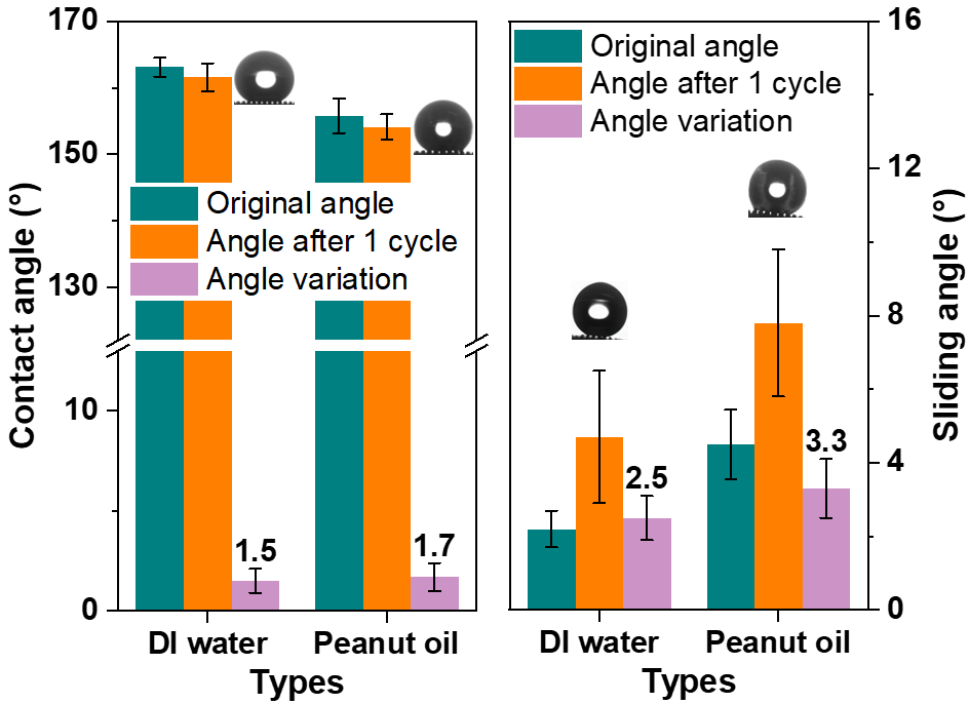

Figure S24. Variations in contact angles and sliding angles for two types of droplets on the MARW surface after icing-melting cycles.

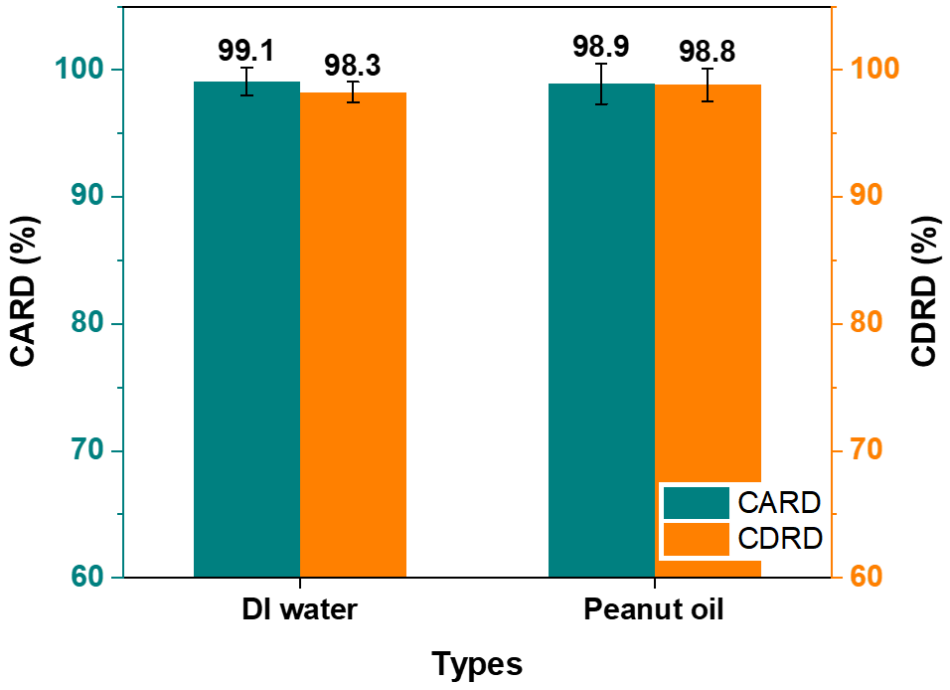

Figure S25. CARD and CDRD of DI water and peanut oil droplets on the MARW surface after icing-melting cycles.

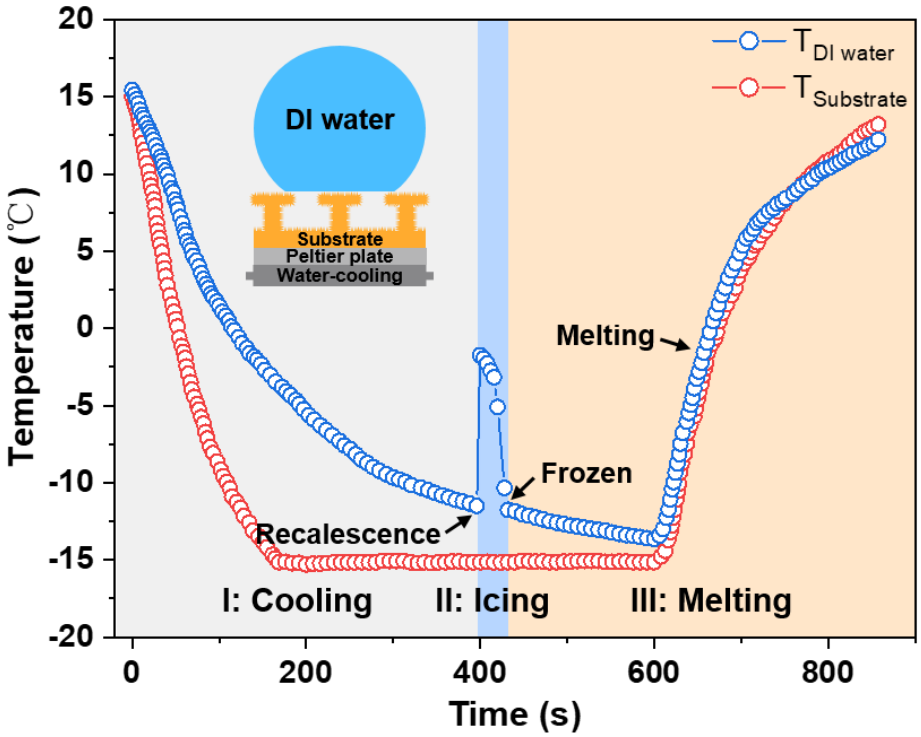

Figure S26. Temperature evolution curve of a DI water droplet during icing on the MARW surface. The surface temperature was rapidly decreased from 15 ℃ to -15 ℃, while the ambient temperature and relative humidity were maintained at 15 ±2 ℃ and 50 ±5% RH, respectively.

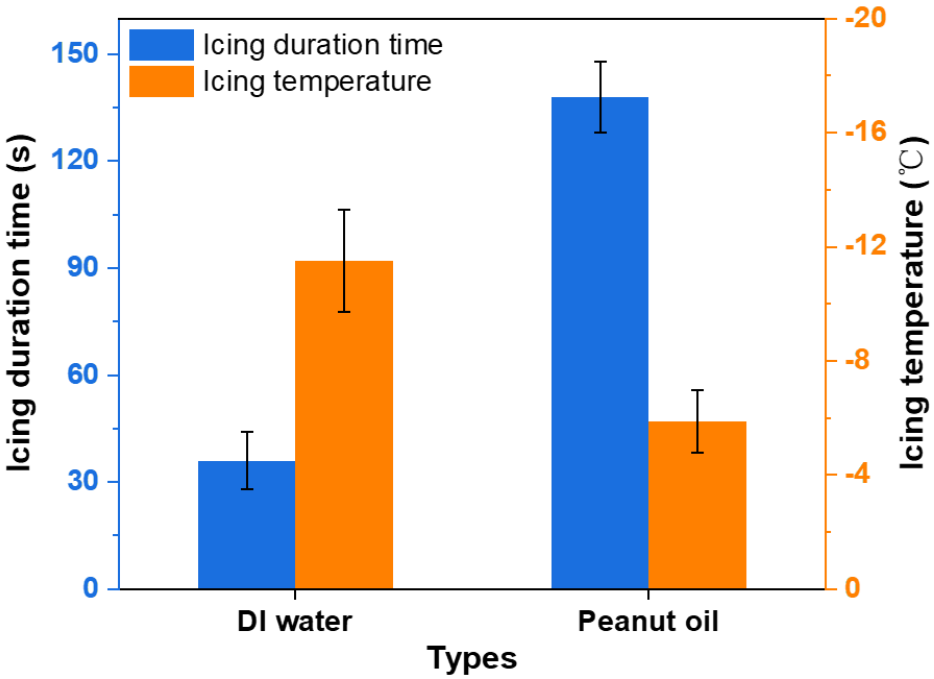

Figure S27. Icing duration time and icing temperature of two different droplets.

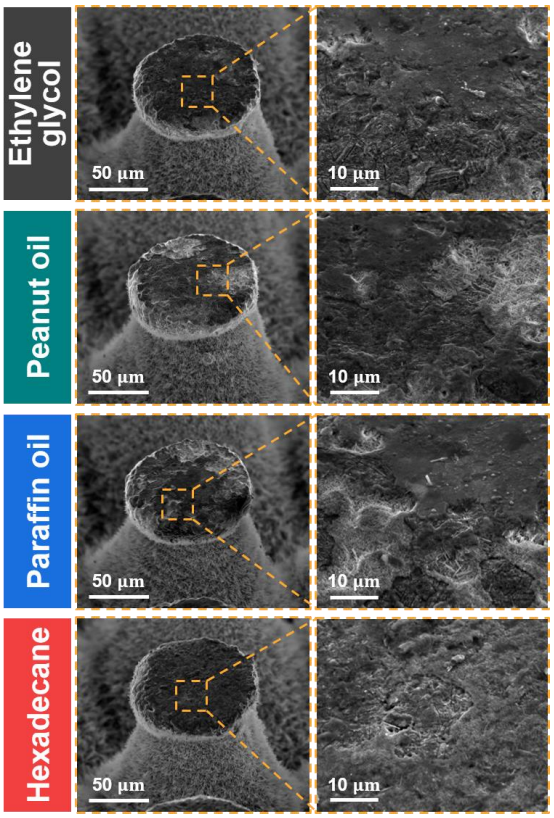

Figure S28. SEM images of the MARW surface after multiple deicing cycles with four organic liquids. The numbers of deicing cycles for ethylene glycol, peanut oil, paraffin oil, and hexadecane were 50, 36, 28, and 14, respectively.

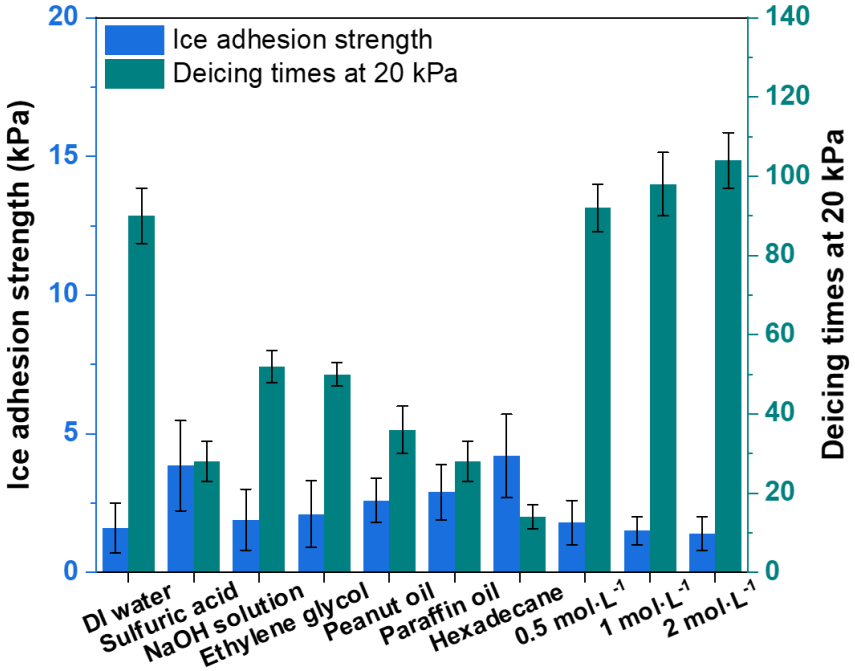

Figure S29. Initial ice adhesion strength and maximum number of deicing cycles below 20 kPa for various liquids on the MARW surface.

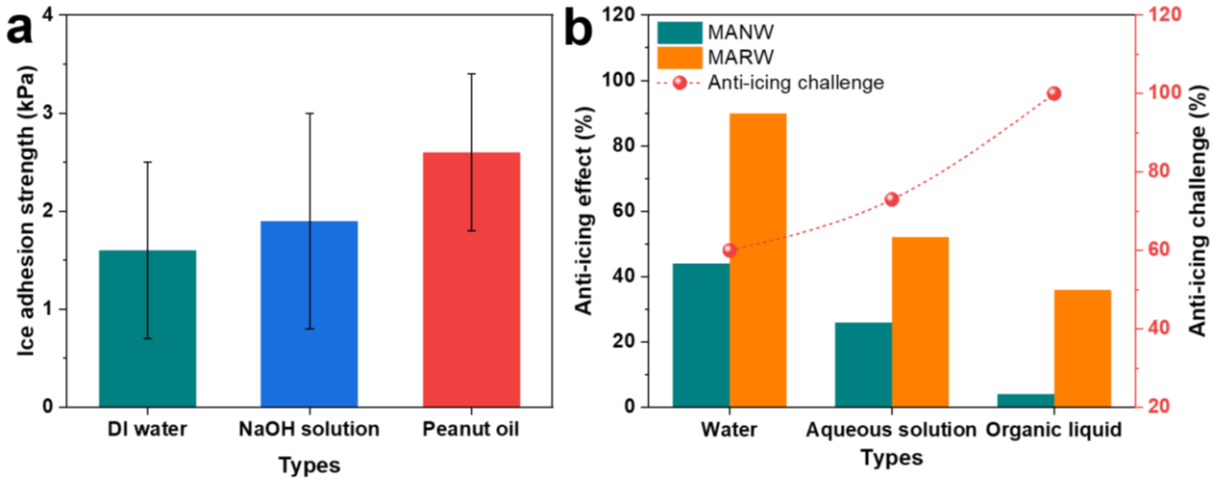

Figure S30. Anti-icing performances of surfaces against various liquids. (a) Ice adhesion strength of DI water, NaOH solution, and peanut oil on the MARW surface. **(b)** Anti-icing effects and challenges of MANW and MARW surfaces. Anti-icing effect is determined by the maximum number of deicing cycles under an ice adhesion strength of $\leq$ 20 kPa, while anti-icing challenge is quantified as the ratio of ice adhesion strengths among the three liquids.

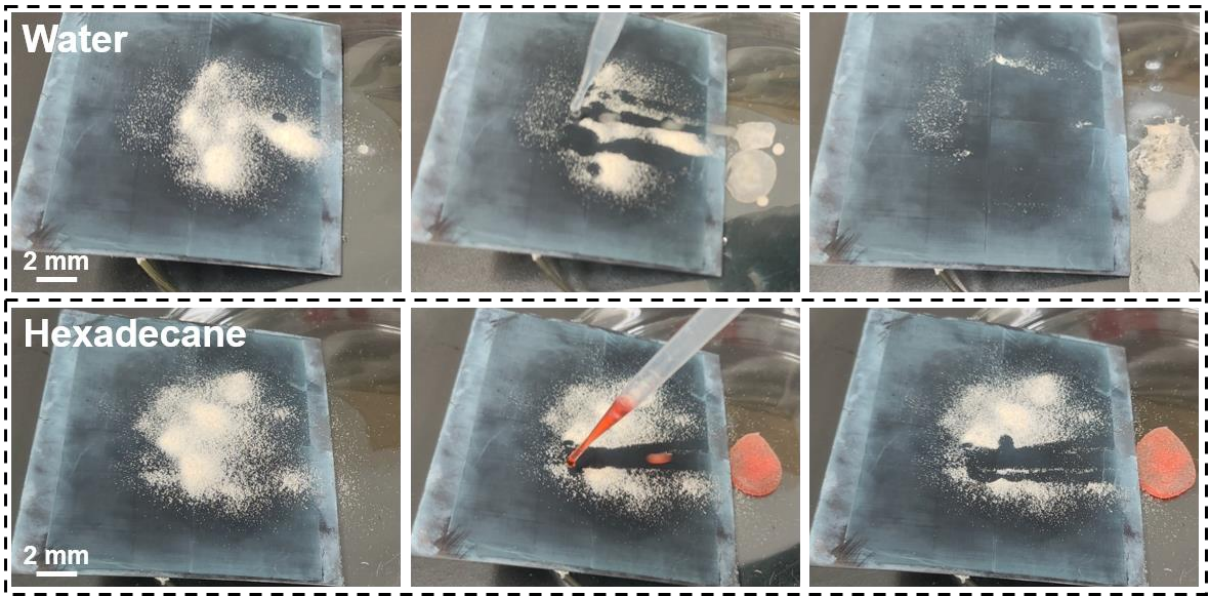

Figure S31. Optical images showing the self-cleaning performance of the MARW surface.

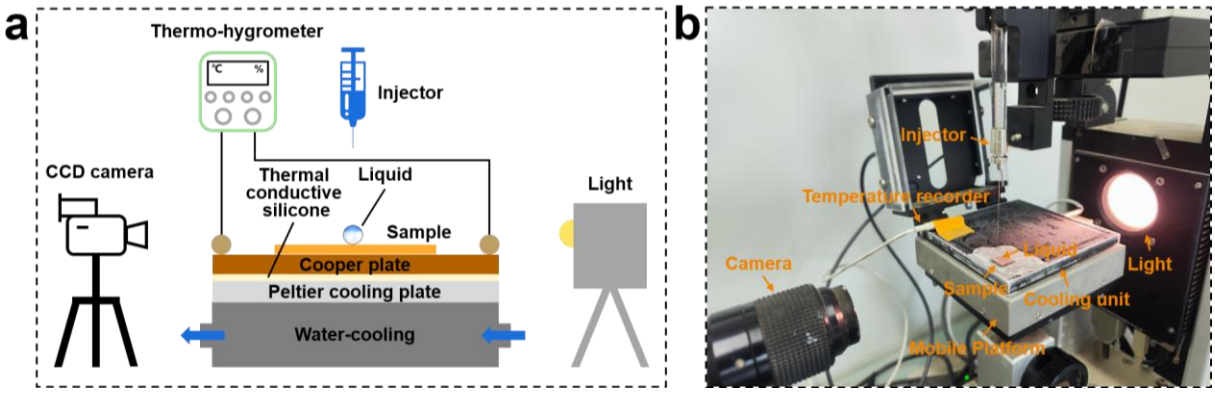

Figure S32. Schematic diagram and photograph of the experimental setup for recording icing and melting processes. (a) Schematic diagram. **(b)** Photograph.

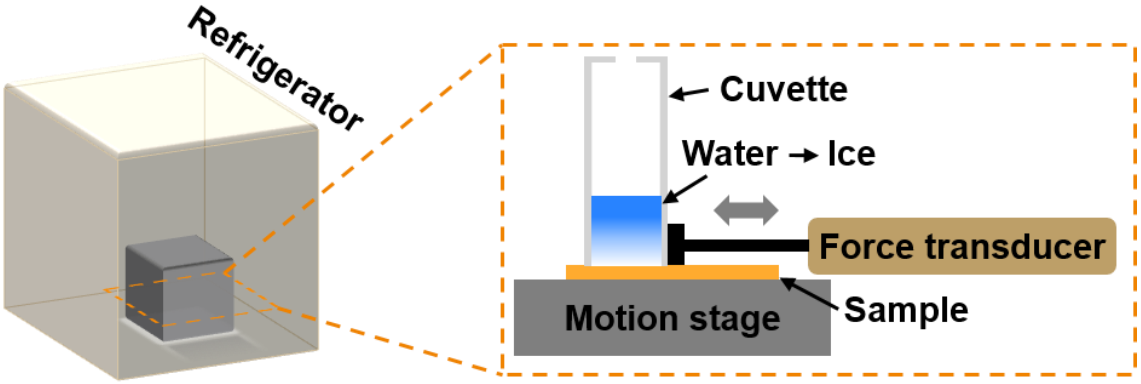

Figure S33. Schematic diagram of the ice adhesion strength measurement setup.

4. Supplementary Videos

Video S1

Deicing processes of sulfuric acid solution on MANW and MARW surfaces.

Video S2

Icing and melting processes of peanut oil droplet on the MARW surface.

Video S3

Icing process of peanut oil droplet on the MARW surface.

Video S4

Mechanical durability tests of the MARW surface.

Video S5

Impact process of sulfuric acid droplet on the MARW surface under low-temperature conditions.

Video S6

Impact process of peanut oil droplet on the MARW surface under low-temperature conditions.

References

1 H. Wu, Z. Yang, B. Cao, Z. Zhang, K. Zhu, B. Wu, S. Jiang and G. Chai, *Langmuir*, 2017, **33**, 407–416.

2 L. Wang, D. Li, G. Jiang, X. Hu, R. Peng, Z. Song, H. Zhang, P. Fan and M. Zhong, *ACS Nano*, 2024, **18**, 12489–12502.

3 Y. Xue, S. Chu, P. Lv and H. Duan, *Langmuir*, 2012, **28**, 9440–9450.